Changing the carbon framework to produce low-expansion silicon-carbon composites for high-performance lithium-ion batteries

Ye Lin[1,2,3], Huang Qiang[1,3,*], Peng Gongchang[2,*], Tian Guilei[3], Bai Hongyou[3], Zhou Xiaoqing[3], Wang Junkuo[3]

(1. *Chengdu Guibao Technology Co., Ltd., Chengdu* 610000, *China*;
2. *Chengdu Organic Chemistry Co., Ltd., Chinese Academy of Sciences, Chengdu* 610000, *China*;
3. *Guibao (Meishan) New Energy Materials Co., Ltd., Meishan* 620860, *China*)

Abstract: Silicon-carbon (Si/C) composites are promising high-capacity anode materials for next-generation lithium-ion batteries, but their commercialization is hindered by their severe volume expansion during cycling. We report a chemical vapor deposition method using the pyrolysis of silane, in which ultrafine nano-Si enters a porous carbon framework to produce kilogram-scale Si/C composites. The carbon framework with abundant micropores (~ 1.9 nm), confines the amorphous silicon and accommodates the volume changes of nano-Si during both lithiation and de-lithiation. The resulting Si/C composites have a 56.76% Si content and have a specific capacity of 2179 mAh g^{-1}, a high initial Coulombic efficiency (ICE) of 93.5%, and a low specific surface area (1.32 m^2 g^{-1}). In addition to the nanoconfinement effect, the median particle size (D_{50}, 7.3-13.0 μm) of the carbon framework was shown to control the mechanical strength, coating uniformity and Li^+ transport. A D_{50} of 8.2 μm endows the Si/C composites with outstanding comprehensive properties. They have an excellent rate performance with a 97.0% retention at 3 C relative to 0.1 C, show only minor variations in ICE difference at 60 ℃/-20 ℃ compared with room temperature, and have a low expansion of 35.8% from the delithiated to the lithiated state. The composite was then mixed with graphite to prepare the anode, which was then paired with an NCM523 cathode to assemble pouch cells. The pouch cell retained 87.46% of its initial capacity after 1000 cycles at 1 C. Because of the low expansion of the electrode, the material avoids structural degradation during cycling and thus has an excellent long-term stability.

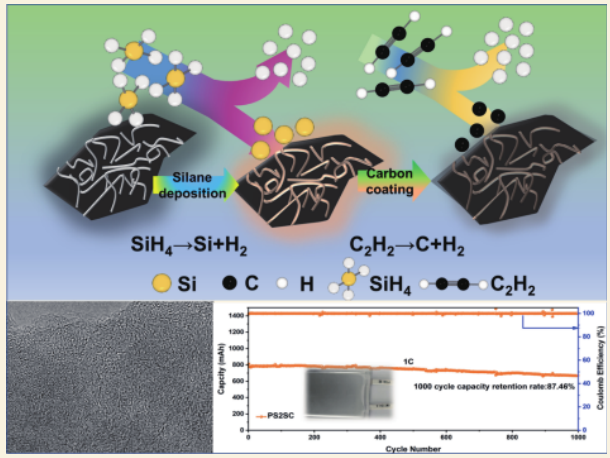

Key words: Si/C composites; Nanoconfinement effect; Micron-scale optimization; Low-expansion; Mass-producible

1 Introduction

To meet the growing demand for high-energy-density lithium-ion batteries (LIBs) in electric vehicles and portable electronic devices, it is urgent to develop advanced anode materials with capacities exceeding that of traditional graphite, which possesses a relatively low theoretical capacity of 372 mAh g^{-1}[1–2]. Among the various candidate anode materials, silicon has attracted considerable attention owing to its exceptionally high theoretical capacity of 3579 mAh g^{-1}, corresponding to the formation of the $Li_{15}Si_4$ alloy phase, and its low lithiation potential (< 0.5 V vs. Li^+/Li)[3–4]. Despite these advantages, the practical application of silicon anodes is hindered by 2 major challenges. First, silicon undergoes a dramatic volume expansion of approximately 300% during lithiation, leading to particle pulverization, electrode structural

Received: February 23, 2026
Revised: May 21, 2026
Accepted: May 22, 2026

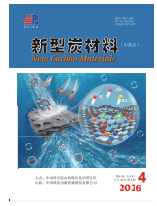

degradation, and rapid capacity fading. Second, its intrinsically low electronic conductivity (~ 10^{-3} S cm^{-1}) and sluggish lithium-ion diffusion coefficient (~ 10^{-12} cm^2 s^{-1}) limit reaction kinetics and rate performance[5–8]. Therefore, addressing these challenges is essential for the large-scale commercialization of silicon-based anodes in next-generation high-energy-density LIBs.

At present, structural engineering is widely regarded as one of the most effective strategies for addressing the challenges associated with silicon-based anode materials, particularly through the development of nanoscale silicon architectures. The particle size of nano-silicon is a critical factor governing its electrochemical performance[9–10]. During lithiation, the substantial volume expansion of silicon can induce severe mechanical stress, leading to particle fracture and structural degradation. Reducing the particle size below the critical fracture threshold (typically <150 nm) can effectively alleviate stress accumulation and suppress pulverization by accommodating volume changes more uniformly. However, excessively small nanoparticles possess a significantly increased specific surface area, which not only deteriorates slurry processability during electrode fabrication but also intensifies undesirable interfacial side reactions with the electrolyte, resulting in excessive solid electrolyte interphase (SEI) formation and reduced Coulombic efficiency[11–12]. Therefore, it is crucial to achieve a balance between volume buffering and interfacial stability through structural design[13]. A comprehensive review systematically articulated that carbon-silicon hybridization could obviously improve silicon anodes, relying on well-designed dimensions and synergistic coupling of both components[8,14]. Optimizing Si/C composite structures focuses on building secondary structures characterized by “nano-scale building blocks, micron-scale integration” that incorporate nano-sized silicon particle units into a carbon matrix to form micron-scale particles with controlled size[15–18]. This design retains the kinetic advantages of the nanoscale while reducing the specific surface area, enhancing mechanical stability, increasing tap density, and improving electrode machinability through an integrated micron-scale structure. Micron-scale secondary particles have also been confirmed to effectively balance swelling buffering, interfacial stability and ion transport[13,19–21]. In particular, based on the fundamental work of Magasinski et al.[22], Group 14 Technologies prepared Si/C composites through a silane pyrolysis route, in which ultra-fine nanoparticles infiltrated into a micron-sized carbon framework matrix, achieving a capacity of over 1800 mAh g^{-1} and an ICE of over 91%. Through strategies such as employing amorphous silicon and implementing nanoscale confinement within the carbon framework, this method effectively produces nanostructured Si/C structures that alleviate diffusion-induced stress and crack, thereby enhancing cycle stability by directly alleviating swelling[20,22–23].

In this work, a scalable kilogram-scale synthesis route was established for the production of high-performance Si/C composites. The composites were fabricated by depositing silicon into a porous carbon (PSC) framework by a silane-based chemical vapor deposition (CVD) process. The PSC framework, characterized by a high specific surface area (2203 m^2 g^{-1}), large pore volume (1.04 mL g^{-1}), and an average pore size of approximately 1.9 nm, enables the deposition of amorphous silicon into its internal pores while effectively restricting silicon growth. The resulting Si/C composites exhibited an ultra-high specific capacity (> 2050 mAh g^{-1}), a high initial Coulombic efficiency (> 93%), and a low specific surface area (< 1.6 m^2 g^{-1}). Furthermore, the effect of micron-scale particle size engineering of the carbon framework was systematically investigated. After optimization of the carbon framework size, the Si/C composite demonstrated excellent rate capability, retaining approximately 97.0% of its capacity at 3 C relative to 0.1 C, as well as robust cycling stability with 80% capacity retention after 100 cycles. More importantly, when assembled into a practical 879 mAh pouch cell using a 550 mAh g^{-1} Si/C-graphite mixture anode paired with an NCM523 cathode, the composite delivered fast electrochemical kinetics, maintaining 87% of its capacity

at 3 C relative to 1 C. It also exhibited excellent long-term durability (87.46% capacity retention after 1000 cycles at 1 C), and excellent low expansion characteristics (＜8% expansion after 1000 cycles). The synergistic integration of nanoscale confinement, silicon amorphization, and micro-scale size control in this work is a key factor for simultaneously achieving high capacity, stable cycling, and low expansion, while also establishing a scalable and industrially viable pathway for large-scale production.

2 Experiment

2.1 Synthesis of Si/C composites

Pulverization and classification of PSC framework: the PSC raw material was pulverized using an air classifier (Q100-2 from Sichuan Shichuang Micro-Nano Technology Co., Ltd.). During the pulverizing process, fine particles smaller than 2 μm are removed by adjusting the parameters, while simultaneously PSC framework materials with D_{50} particle sizes of 7.3, 8.2, 10.3, and 13.0 μm were obtained (Table S1), and the pulverized products were sequentially named PS1C, PS2C, PS3C and PS4C.

Preparation of Si/C precursors: 1.5 kg of PS1C was adding into the kilogram-scale fluidized bed chemical vapor deposition (FBCVD) reactor. Under N_2 atmosphere, the FBCVD reactor was then heated at a rate of 5 °C min^{-1}. When the temperature reached 490 °C, the silane (SiH_4) gas was fed into the FBCVD reactor for deposition of Si in the PS1C carbon framework. After 14.7 hours of deposition, the supply of SiH_4 was stopped, with the ratio of SiH_4 volume to PS1C mass reaching 1100 L kg^{-1}. After that, the FBCVD reactor was heated up to 580 °C at a rate of 2 °C min^{-1}. Then, the acetylene (C_2H_2) gas was then introduced for 1.5 hours to perform carbon coating treatment, with the ratio of C_2H_2 volume to PS1C mass being 184.7 L kg^{-1}. Finally, the final products was obtained 3.7 kg and named PS1C/Si. By replacing PS1C framework with PS2C, PS3C and PS4C in sequence and repeating the above process, the corresponding materials PS2C/Si, PS3C/Si and PS4C/Si were obtained respectively. The PS2C/Si, PS3C/Si, and PS4C/Si samples were all controlled to an output mass of ~ 3.7 kg.

Secondary carbon coating: The PS1C/Si power with a mass of 2 kg was transferred into a kilogram-scale CVD batch furnace. Under N_2 atmosphere, the furnace was heated at a rate of 5 °C min^{-1}, until the temperature rose to 580 °C. Then C_2H_2 gas was fed for 5 h for secondary carbon coating, at which the ratio of the volume of C_2H_2 to the mass of PS1C/Si reached 225 L kg^{-1}. After natural cooling, the obtained Si/C anode material was discharged and named PS1SC. Following the same coating procedure, by replacing PS1C/Si with PS2C/Si, PS3C/Si and PS4C/Si in sequence, the corresponding PS2SC, PS3SC and PS4SC were prepared, respectively. After the secondary carbon coating, the mass of the obtained products are approximately 1.9 kg owe to the tendency of fine powder to be blown away.

2.2 Material characterization

The particle size of the materials was measured using a Mastersize 3000. The powder resistivity of the samples was determined with a MODEL FZ-2010. X-ray diffraction (XRD) patterns were recorded on a Bruker D8 ADVANCE diffractometer (λ = 1.5418 Å). The individual crushing force of the materials was tested via an SPFT1000. Raman spectra were collected using an XploRA Plus spectrometer. The morphology and structure of the materials were characterized by high-resolution Thermo Scientific Helios 5 CX and high-resolution Apreo 2C HiVac scanning electron microscope (SEM). The crystal plane information of the samples was acquired using a JEOL JEM-2100F transmission electron microscope (TEM). Nitrogen adsorption-desorption experiments were conducted on a BSD-660M. The pore size distribution of the samples was determined by the nonlocal density functional theory (NLDFT) method, and the specific surface area was calculated according to the Brunauer-Emmett-Teller method. The cross-sectional morphology of porous carbon and Si/C composites were characterized using a Hitachi IM4000II ion milling system and SU3800SE SEM.

3 Results and discussions

3.1 Physiochemical characterization and analysis

To achieve spatial nanoconfinement, a highly microporous-rich carbon framework was employed as the host material. To attain high capacity, a substantial silicon loading was targeted, thereby requiring a high pore volume to accommodate silicon incorporation[24]. Consequently, a resin-derived PSC raw material with high pore volume was selected. As shown in Fig. S1, the porous carbon before broken exhibits rough spherical particles ranging from 50 to 130 μm in diameter, with finer spheres fused within the structure. To investigate the effect of micron-scale size on the performance of Si/C anodes, sphere-shaped PSC raw material was jet-milled to obtain 4 variants with distinct particle sizes. Based on the particle-size distributions (Fig. S2) and the data summarized in Table S1, the D_{50} values of the 4 porous carbons are tuned to the values of ~ 7.3, 8.2, 10.3 and 13.0 μm, corresponding to PS1C, PS2C, PS3C and PS4C carbon frameworks, respectively. Notably, although all four porous carbons exhibited unimodal particle-size distributions, particles smaller than 2 μm were intentionally removed to minimize agglomeration and ensure stable fluidization during the subsequent fluidized-bed silicon deposition process. The N_2 adsorption-desorption isotherms and pore-size distributions (Fig. S3) reveal that these PS1C, PS2C, PS3C and PS4C carbon frameworks exhibit Type-I isotherms, indicating a predominantly microporous structure. Moreover, these materials possess similarly high pore volumes (1.0-1.05 mL g^{-1}) and specific surface areas (2200-2230 m^2 g^{-1}) (Table S2). The high surface energy facilitates the adsorption of SiH_4 molecules and heterogeneous nucleation, and these structural characteristics of high pore volume provide abundant accessible pore sites for Si loading[25]. Importantly, these samples maintain a consistent average pore width of 1.82−1.89 nm and a high micropore ratio of 88.2%−91.5%, ensuring effective nanoconfinement during Si deposition and resulting in ultra-fine Si particle sizes, which is conducive to reducing Si particle expansion during the lithiation process[26−27]. Notably, only pores larger than the kinetic diameter of SiH_4 molecules (~ 0.408 nm) are accessible for SiH_4 diffusion, which indicates that the pore structure in the selected PSC meets this requirement. Overall, the four porous carbon frameworks exhibit significant differences in particle size, while maintaining comparable pore characteristics. This controlled variation enables a systematic study of how micron-scale particle size influences material performance, isolating it as the primary variable for optimization.

To evaluate the impact of particle size, these four composites were processed under identical fluidized-bed conditions, with the same feed amount and operating parameters. The synthesis of the Si/C composites is illustrated in Fig. 1a. PSC framework was first subjected to silicon deposition by FBCVD reactor at 490 °C ($SiH_4 \rightarrow Si + H_2$). The resulting material was then initially carbon-coated in a FBCVD reactor at 580 °C via using C_2H_2 gas as the carbon source, yielding intermediate products. Subsequently, these intermediates underwent a secondary carbon coating in a rotary furnace at 580 °C via using C_2H_2 gas as the carbon source. Finally, four Si/C composites were prepared and named PS1SC, PS2SC, PS3SC and PS4SC, and the D_{50} particle size of Si/C composites are 7.5, 8.4, 10.9 and 13.4 μm (Fig. 1b), respectively. The particle sizes match the trend of the original PSC framework, together with a slight increase. Although the resulting Si/C material has a weight increase of about 147% compared to PSC, Fig. 1b shows that the particle size of the Si/C composite is only slightly increased, still maintaining a particle size close to that of the PSC framework, indicating that Si nanoparticles are deposited within the pores rather than on the outer surface.

The synthesized PS1SC, PS2SC, PS3SC and PS4SC composites were characterized by XRD (Fig. 1c). Notably, this series of broad diffraction humps at ~ 28° which correspond to the (111) plane of Si (PDF#27-1402), indicate that the nano-Si in the highly microporous-rich PSC frameworks is predominantly amorphous[28]. Compared with crystalline silic-

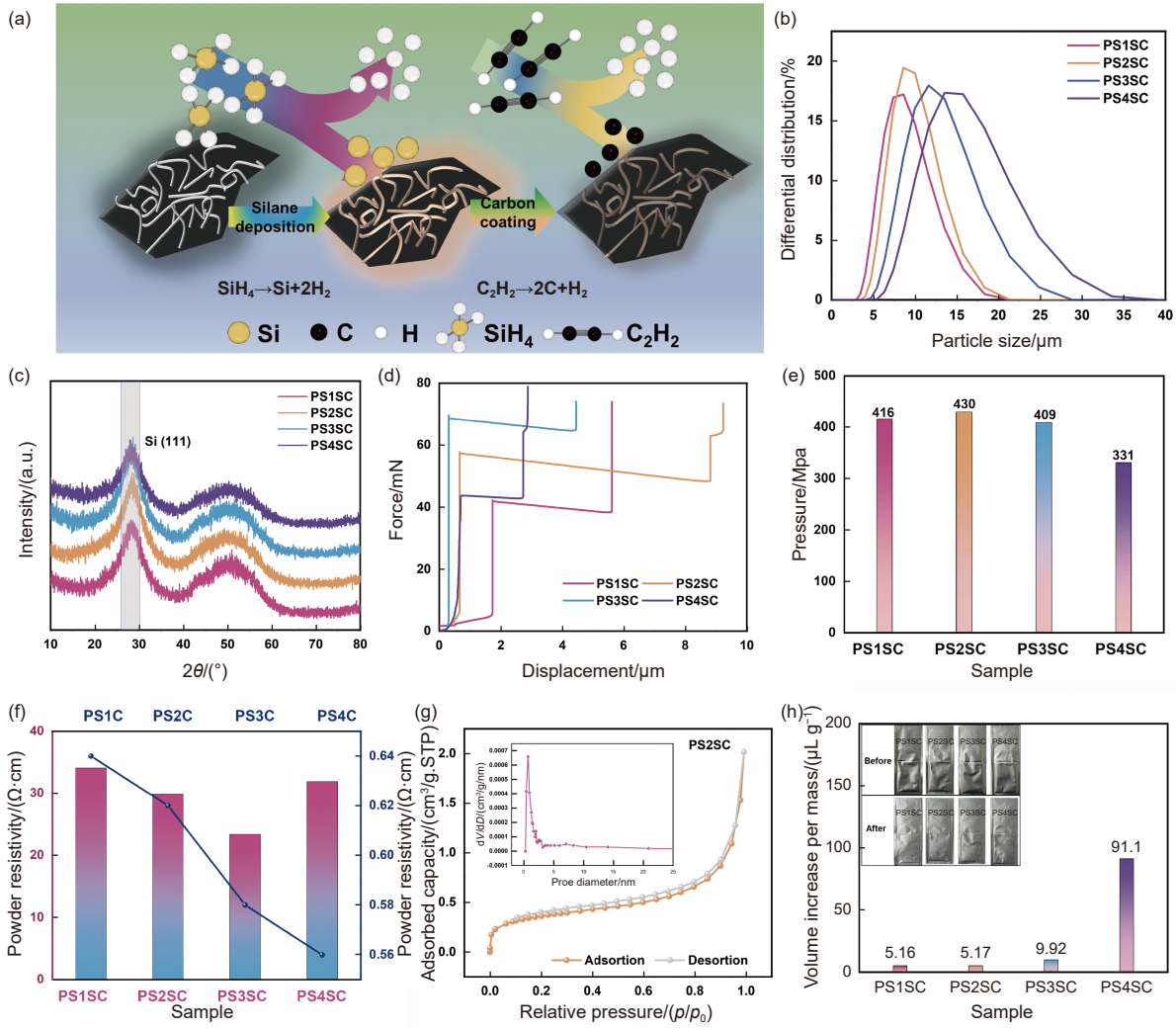

Fig. 1 (a) Schematic diagram of the synthesis process for Si/C composites. (b) Particle size curves of PS1SC, PS2SC, PS3SC and PS4SC. (c) X-ray diffraction spectra of PS1SC, PS2SC, PS3SC and PS4SC. (d) Force-displacement curves of PS1SC, PS2SC, PS3SC and PS4SC. (e) Pressure crushing strength of PS1SC, PS2SC, PS3SC and PS4SC. (f) Powder resistivity of PS1SC, PS2SC, PS3SC and PS4SC material and its corresponding porous carbon. (g) N_2 adsorption-desorption isotherm curves and pore size distributions of PS2SC. (h) Gas production of PS1SC, PS2SC, PS3SC and PS4SC placed at 60 °C for 24 h (inset shows photos of Si/C materials placed in the mold before and after gas production)

on, amorphous silicon exhibits significant ultrafine particle size (lower than the pore size of the porous carbon framework) and isotropic expansion behavior, which will all help mitigate volume changes during cycling, thereby enhancing the cycle stability of the material[29–30] . The carbon content of these 4 Si/C composites was measured using a muffle furnace at 980 °C, and the silicon content was calculated. As described in the Experimental Section, the Si/C composite is fabricated by high-temperature silane pyrolysis in a fluidized bed to deposit silicon inside porous carbon, followed by primary carbon coating in the fluidized bed and secondary carbon coating in a rotary furnace. After primary coating, the Si content (Si content measured in mass percentage) of PS1C/Si, PS2C/Si, PS3C/Si and PS4C/Si are 55.28%, 57.37%, 55.34% and 57.69%, respectively (Fig. S4a). After secondary carbon modification, the Si contents of PS1SC, PS2SC, PS3SC and PS4SC decrease to 54.08%, 56.76%, 53.52% and 56.15% (Fig. S4b), with a reduction of 1.20%, 0.61%, 1.82% and 1.54%. For PS2SC composites, the low reduction of 0.61% indicates a lower acetylene conversion rate and a slower carbon layer growth rate during carbon coating, which may be conducive to a more uniform carbon coating.

The mechanical strength of the Si/C composites directly affects the compressibility of the Si/C composites and its ability to resist expansion during lithi-

um intercalation process, which are closely linked to their compaction density and long-term cycling performance. The mechanical strength of these Si/C composites with different particle sizes was measured by a single particle crush tester. In Fig. 1d and e, the sharp rise in displacement indicates particle fracture, and the compressive strength is calculated from the force at failure and the corresponding effective bearing area[31]. The crushing strengths of PS1C, PS2C, PS3C and PS4C were measured to be 270, 236, 195 and 133 MPa, respectively (Fig. S5a and b), confirming that particle size has a negative correlation with crushing strength. After Si deposition and carbon coating, the strengths were determined to be 416, 430, 409 and 331 MPa, respectively (Fig. 1d,e). The higher crushing strength was observed for both PS2C and corresponding Si/C composites at ~ 8 μm, whereas deteriorated strength was exhibited for both PS4C and corresponding Si/C composites at ~ 13 μm. Therefore, both the particle size of initial porous carbon and the preparation process of Si/C composites have a certain influence on the crushing strength. Among these materials, PS2SC showed the highest crushing strength (430 MPa), indicating its more excellent mechanical stability and deformation resistance.

The powder resistivity of different carbon framework and corresponding Si/C composites was tested and compared. In Fig. 1f, the powder resistivity of the carbon framework ranges from 0.56 to 0.64 Ω·cm. After Si deposition and carbon coating, the corresponding composites of PS1SC, PS2SC, PS3SC and PS4SC exhibited significantly higher values of 34.1, 29.9, 23.4 and 31.9 Ω·cm, respectively. This significant increase confirms the successful Si nanoparticle deposition. Furthermore, all powder resistivity values of Si/C composites remained below 1000 Ω·cm, indicating that most Si nanoparticles were located within the micropores of the carbon framework[32]. The tap density values of these Si/C composites were measured using a tap densitometer (Fig. S6) and reached 1.02, 0.99, 0.99, 1.00 g cm^{-3}, thus ensuring good slurry processability during stirring[33]. The N_2 adsorption-desorption isotherms (Fig. 1g) and pore-size distributions (Fig. S7) of the Si-C composites indicate a Type-IV mesoporous structure. With the size increase from PS1SC to PS4SC, the specific surface areas and pore volumes decrease gradually to 1.58, 1.32, 1.07, 0.95 $m^2 g^{-1}$, and to 0.0033, 0.0030, 0.0025, 0.0024 mL g^{-1}, respectively. This sharp reduction in the specific surface area and pore volume from the PSC framework to the Si/C composite confirms that the Si nanoparticles and carbon layers have filled the internal micropores of the PSC framework, leaving negligible external mesopores. The resulting ultra-low surface area (<2 $m^2 g^{-1}$) benefits slurry processing by reducing gas evolution ($Si + 3H_2O \rightarrow 2H_2\uparrow + H_2SiO_3$) and enhances electrochemical stability by minimizing surface side reactions. To evaluate the integrity of the carbon coating, the slurry of Si-C composites was sealed in an aluminum foil bag and stored at 60 °C for 24 h for gas-evolution testing[34–35]. In Fig. 1h, the foil bag did not show obvious expansion, indicating that the surface gas production of the 4 materials was less, showing a good carbon coating effect of Si/C composites. The gas generation calculated from the density change of the aluminum foil bag measured by a solid densitometer was 5.16, 5.17, 9.92 and 91.1 μL g^{-1}, respectively, which are far below the processability standard of the Si/C composites (150 μL g^{-1}). This shows that the gas production of Si/C materials with larger particle size will slightly increase under the same material synthesis process conditions, and the smaller particle size also means better carbon layer coating.

In Fig. 2a, Raman spectra of these Si/C composites display a peak at ~ 450 cm^{-1} corresponding to amorphous silicon, with no detectable signal near 510 cm^{-1}, further confirming the amorphous feature of the Si nanoparticles[36]. The characteristic *D* and *G* bands of carbon appear at 1326 and 1591 cm^{-1}, inversely related to graphitization and defect density. Among them, PS2SC has the lowest I_D/I_G value of 0.826, indicating that its defect density is low and its structural order is high, which will help to improve its charge and discharge efficiency and cycle structural stability. The 2D Raman diagram (Fig. 2b-d, S8) shows the

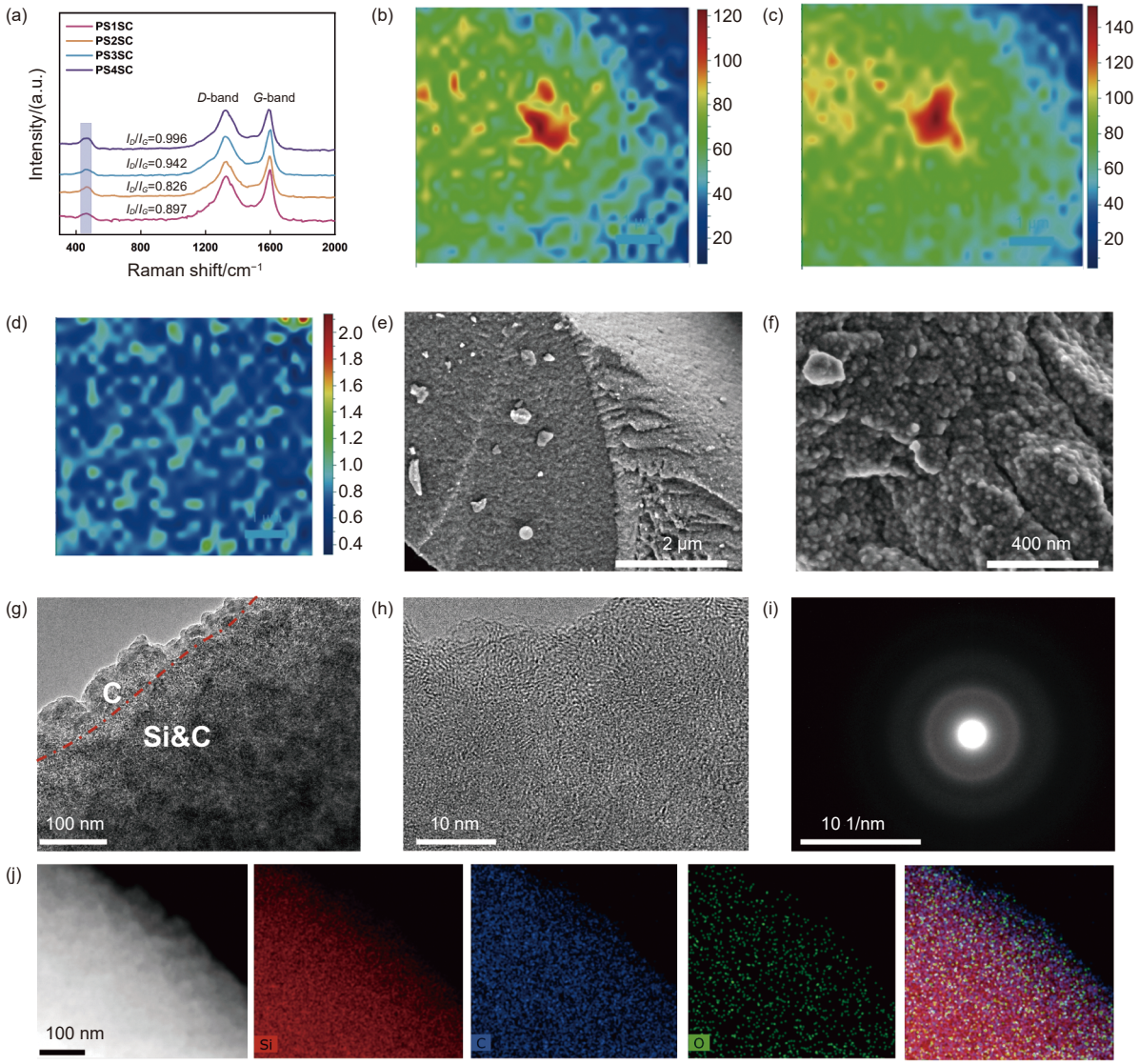

Fig. 2 (a) Raman spectra of PS1SC, PS2SC, PS3SC and PS4SC. (b-d) *D* bond signal, *G* bond signal and I_D/I_G Raman mapping spectra of PS2SC. (e,f) SEM images of PS2SC at low voltage. (g-i) TEM, HRTEM, and SAED images of PS2SC. (j) TEM image of PS2SC and corresponding EDS element mapping images of Si, C and O elements

minimum spatial variation of I_D/I_G signal in the whole PS2SC sample, reflecting the absence of agglomeration or segregation phenomenon in the Si/C material[37]. Accordingly, the specific surface areas of these Si/C composites are controlled below 2 m^2 g^{-1}, proving that the carbon layer can effectively encapsulate silicon particles. Meanwhile, the lower I_D/I_G value of 0.826 and the limited gas evolution further verify that the PS2SC composites possess a dense carbon coating and fewer structural defects.

The morphologies of the four materials are shown in the SEM images of Fig. S9. PS1SC, PS2SC, PS3SC and PS4SC exhibited similar irregular block-like structures, and the micro-scale size was from small to large, which is consistent with the particle size test. To resolve the finer surface details of the carbon coating, a low-voltage SEM was used, providing higher resolution and minimizing sample damage. As shown in Fig. 2e and 2f, the surface of PS2SC is uniformly covered with a dense, island-like carbon layer. These island-like carbon, merely several tens of nanometers in size, are densely packed to effectively seal the residual pores. This carbon coating enhances electrical conductivity and isolates direct contact between silicon and electrolyte, thus effectively reducing side reactions[38].

To investigate the internal structural and compositional changes of Si/C composites before and after silicon deposition, the PS2C porous carbon and Si/C composites were bonded with conductive adhesive and processed by argon ion polishing to obtain intact cross-sections. Fig. S10a-b present the cross-sectional SEM images and corresponding element mapping of PS2C porous carbon. The PS2C exhibits densely and uniformly distributed internal structure. Although PS2C exhibits a high pore volume of 1.04 mL g^{-1}, no obvious pore structures can be observed in the SEM images. This is attributed to the predominance of micropores, whose dimensions are below the resolution limit of conventional SEM. As shown in Fig. S10c-f, elemental mapping reveals strong C and O signals, while no silicon signal is detected. The abundant microporous structure provides a favorable framework for the subsequent deposition and confinement of silicon species. Fig. S11a-c display that PS2SC maintains the original cross-sectional structural characteristics of PS2C. Corresponding cross-sectional element mappings (Fig. S11d-h) further verify that Si element is uniformly dispersed throughout the entire particle cross-section. No surface enrichment of Si or continuous Si core is observed. Therefore, amorphous Si nanoparticles deposit uniformly inside the internal pores of porous carbon, rather than just adsorbing on the particle surface or forming a macroscopic core-shell structure. In addition, Fig. S11c shows a carbon coating layer with a thickness of 44−76 nm on the surface of PS2SC. This layer not only provides structural confinement and physical buffering for the Si-C composites, but also effectively isolates nano-Si from direct contact with air.

Fig. 2g shows the TEM image of the PS2SC material. It can be seen that the surface of the material is a carbon layer structure, which isolates the internal Si/C composite from the external environment, so that the internal nano-Si will not directly react with the external air. In Fig. S11(e−f), Si and C elements are uniformly distributed within the interior of PS2SC particles, the non-particulate carbon signal originates from the conductive adhesive used during argon ion polishing, which further confirms the integrated Si/C composite structure in the interior of PS2SC. Meanwhile, the outer region shows an intense carbon signal and a weak Si signal, verifying the successful surface carbon coating. Accordingly, PS2SC possesses an internal Si/C composite structure and an external carbon layer. No obvious long-range ordered atomic arrangement in the material was observed in the HRTEM image of Fig. 2h, where the atoms were randomly distributed without obvious periodicity. Moreover, the selected area electron diffraction (SAED) pattern also shows a set of scattered ring structures (Fig. 2i). All these confirm that nano-Si exist in amorphous structure in the material, which are consistent with the results of XRD and Raman test. The element distribution results in Fig. 2j show that the Si, C and O elements in the material are uniformly distributed, indicating that the material progresses uniformly during silicon deposition and carbon coating without segregation.

Overall, based on the same PSC framework with different particle sizes, all have abundant microporous structures to accommodate high Si loading and spatially constrain the deposited nanosilicon. The four Si/C composites synthesized by the same process of silane and acetylene pyrolysis all have similar characteristics, such as high silicon content, low specific surface area, and amorphous silicon carbon confinement. It is worth noting that the PS2SC material shows better mechanical strength and coating effect, which is the result of the size difference of porous carbon raw materials.

3.2 Electrochemical analysis

In Fig. 3a, the half cell was assembled to evaluate the effect of particle size on the electrochemical performance of 4 Si/C composites. A four-step discharge protocol (discharged to 5 mV at rates of 0.1 C, 0.05 C, 0.025 C and 0.01 C, respectively) was applied during the discharge process to ensure the full lithiation of active material, then charged to 2 V at a current density of 0.1 C. In Fig. 3b, the first-cycle specific capacities of PS1SC, PS2SC, PS3SC and PS4SC were 2102, 2179, 2069 and 2165 mAh g^{-1}, which cor-

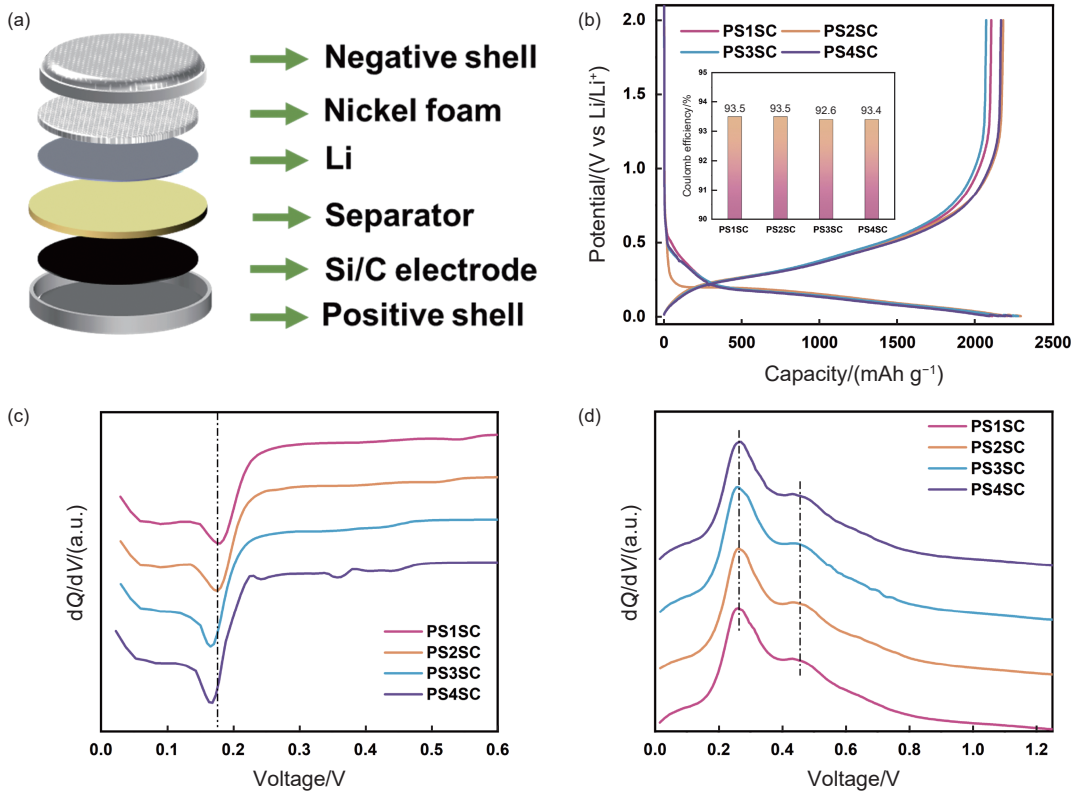

Fig. 3 (a) Schematic diagram of LIR2016 type coin cell. (b) Initial discharge-charge capacity curves for PS1SC, PS2SC, PS3SC and PS4SC (inset is the first coulombic efficiency of the battery) (c, d) The initial discharge and charge dQ/dV curves of PS1SC, PS2SC, PS3SC and PS4SC, respectively

relate positively with ultra-high silicon content (55.5% ± 1.5% for these Si/C composites). The PS1SC, PS2SC, PS3SC and PS4SC electrodes displays ultra-high ICE values of 93.5%, 93.5%, 92.6% and 93.4%, which is attributed to the well-controlled deposition and effective CVD coating, which reduces specific surface area and surface oxidation. These results suggest that particle size has little impact on ICE values.

The initial discharge-charge capacity was differentiated to the amount of voltage to obtain the corresponding dQ/dV-V curves (Fig. 3c, 3d and S12). In Fig. 3c, during the initial lithiation process of these four Si/C electrodes, characteristic redox peaks reveal the phase evolution of silicon. In the lithiation process, a series of peaks at ~ 0.17 V correspond to the transformation from Si to amorphous Li-Si alloy, and the reduction peaks at ~ 0.06 V correspond to the transition from amorphous Li-Si alloy to crystalline $Li_{3.75}Si$. Correspondingly, the delithiation dQ/dV-V curves in Fig. 3d exhibits the peaks near 0.26 and 0.46 V, which are attributed to the reversal transformations of amorphous $Li_{3.5\text{-}3.75}Si$ and crystalline $Li_{3.75}Si$ back to the amorphous Li-Si alloy, respectively. Notably, the wide peaks at 0.46 V for these Si/C composites, is clearly linked to the low crystallinity observed before lithiation[39–40]. To compare the polarization of the four samples with different particle sizes, we also compared the peak shifts of dQ/dV-V curves during delithiation and lithiation. It can be seen that as the particle size of Si/C composites increases from 7.5 to 13.4 μm, the reduction peaks gradually shift to a lower voltage and the oxidation peaks gradually shifts to a higher voltage, indicating that the larger particle size of Si/C composites is detrimental to the fast lithiation/delithiation kinetics and aggravates electrode polarization.

For further evaluate the effect of particles size on lithiation/delithiation kinetics of Si/C anodes, the PS1SC, PS2SC, PS3SC and PS4SC composites were each blended with graphite (Fig. S13) to achieve similar specific capacities of 920 ± 30 mAh g^{-1} (Fig. S14a), named PS1SC&Gr, PS2SC&Gr, PS3SC&Gr, PS4SC&Gr electrodes, respectively. The similar spe-

cific capacities contribute to evaluate their respective effects on delithiation/lithiation kinetics, high-temperature side reactions, and low-temperature kinetic performance. The PS1SC&Gr and PS2SC&Gr electrodes exhibit significantly higher capacity retention rates under high-rate charging, and their capacities are 912 and 915 mAh g^{-1} at a current of 0.1 C as shown in Fig. S14b, respectively, 97.97% and 97.35% at a current of 1 C, and can still reach 97.21% and 96.95% at a current of 3 C as shown in Fig. 4a. In contrast, the capacity retention rate of PS4SC&Gr electrode with larger particles is only 95.43% when the current is 3 C. To further demonstrate the differences between the electrode sheets, we conducted a comparative analysis of the average de-lithiation voltage (the ratio of de-lithiation energy to capacity) at different rates for PS1SC&Gr and PS2SC&Gr electrodes, as shown in Fig. 4b. At de-lithiation of 0.1 C rate, the differences were not significant. Even as the discharge rate progressively increased from 0.1 C to 3 C, the average potential of PS1SC and PS2SC&Gr electrodes remained at a relatively low level. At 1 C and 3 C, the potential increase of PS1SC&Gr and PS2SC&Gr electrodes compared to 0.1 C was 0.05V/0.14V and 0.05V/0.15V, which is notably lower than that of PS3SC (0.07V/0.17V) and PS4SC (0.08V/0.18V).The lower de-lithiation potential under high current conditions indicates superior de-lithiation kinetics.

By analyzing the proportion of the high-current step capacity to the total four-step discharge capacity

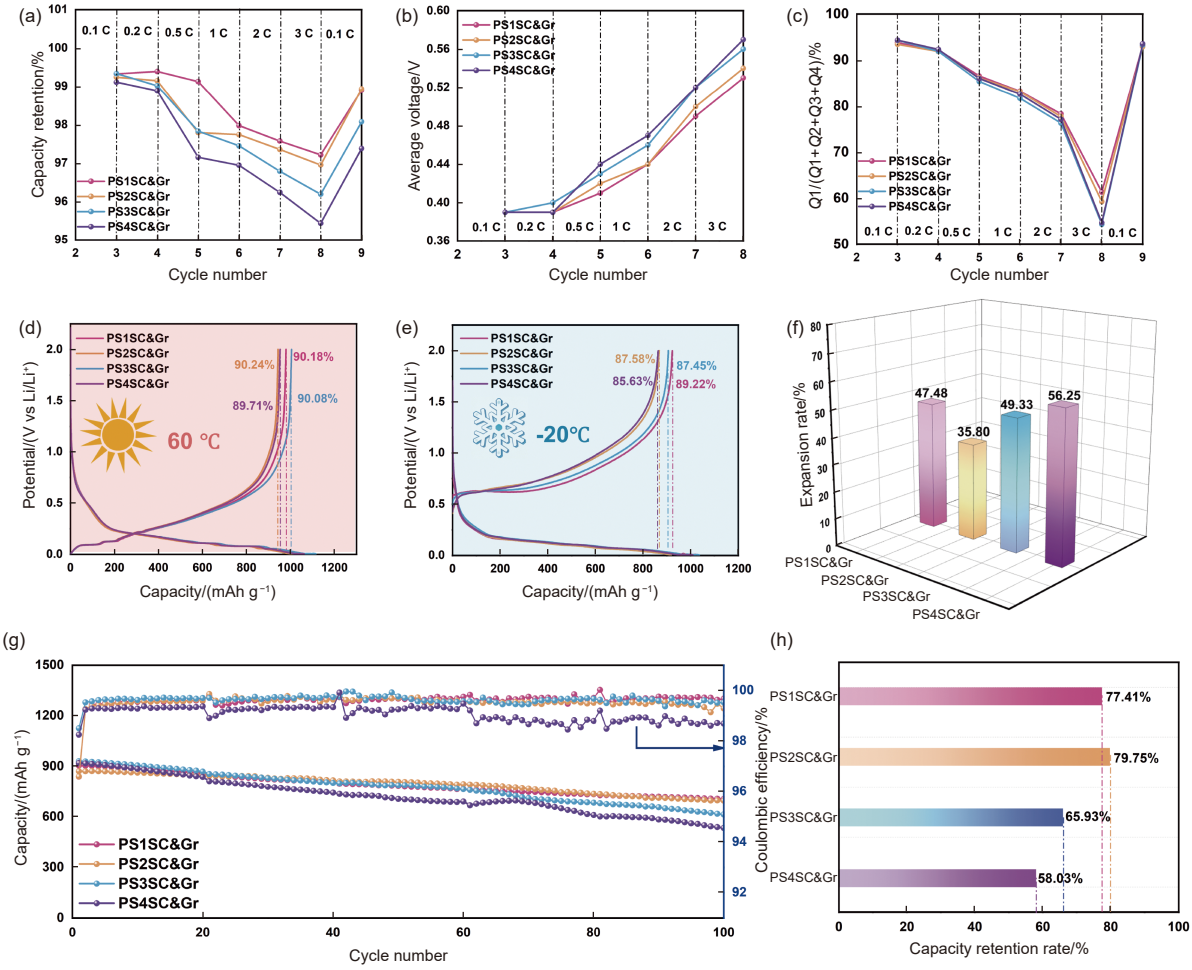

Fig. 4 (a−b) Capacity retention and average voltage curves for the rate performance of different materials. (c) The large current capacity accounts for the proportion of the overall discharge capacity when discharging at different rates of materials. (d) Charge-discharge curves of different materials at 60 °C. (e) Discharge at 25 °C and charge curves at −20 °C for different materials. (f) 5 mV lithium intercalation expansion performance of pole pieces with PS1SC&Gr, PS2SC&Gr, PS3SC&Gr and PS4SC&Gr. (g) Cycle performance and (h) capacity retention curves of 100 cycles of half-cell cycles for PS1SC&Gr, PS2SC&Gr, PS3SC&Gr and PS4SC&Gr

($Q1$/($Q1$+$Q2$+$Q3$+$Q4$)) at different current densities, the lithiumation capability of the material can be determined. As shown in Fig. 4c and S14c, the high-current capacity of PS1SC&Gr and PS2SC&Gr electrodes at a 3 C current density was 553.37 and 520.45 mAh g^{-1}, respectively, accounting for 65.24% and 61.36% of the total discharge capacity. These values were significantly higher than those of PS3SC&Gr and PS4SC&Gr electrodes. The anode material is more prone to undergo side reactions with the electrolyte under high-temperature testing, leading to the thickening of SEI membrane and increase of internal resistance, which ultimately results in a decrease in specific capacity and ICE[41]. Fig. 4d displays the charge-discharge tests of PS1SC&Gr, PS2SC&Gr, PS3SC&Gr and PS4S&Gr electrodes in a 60 °C environment. The ICE values of charge-discharge tests of PS1SC&Gr, PS2SC&Gr, PS3SC&Gr and PS4SC&Gr electrodes were found to be 90.18%, 90.24%, 90.08% and 89.71%, respectively. By contrast, the ICE values of these electrodes at room temperature remain above 93.0% (Fig. S14a). The ICE values at 60 °C test show a significant decay of ~ 3%, indicating a general increase in side reactions. It is evident that PS1SC&Gr and PS2S&Gr electrodes exhibit slightly higher ICE values, which suggests that more stable electrode/electrolyte interface, which will effectively improve the cycle life and safety of the battery.

Simultaneously, the low-temperature delithiation kinetics of these electrodes were compared by discharging at room temperature and then charging at −20 °C. In Fig. 4e, the corresponding ICE values of PS1SC&Gr, PS2SC&Gr, PS3SC&Gr and PS4S&Gr electrodes at −20 °C were 89.22%, 87.58%, 87.45% and 85.63%, respectively. The Fig. S14a and 4e show that the discharge process was maintained at room temperature to ensure sufficient lithiation, while the charge curves at −20 °C exhibited significantly higher potentials and pronounced polarization compared with the charge curves at room temperature, which hindered adequate delithiation and led to a substantial deterioration in ICE. Nevertheless, the extent of deterioration varied among the samples. Compared to their initial room-temperature ICE values, PS1SC&Gr, PS2SC&Gr, PS3SC&Gr and PS4S&Gr electrodes show deteriorations of 4.46%, 5.62%, 6.15% and 7.73%, respectively. Regarding particle size effects, particles with a diameter of 7.5 μm demonstrated the best kinetic performance, while those of 8.4 and 10.9 μm exhibited comparable results. However, when the particle size increased to 13.4 μm, the ICE deteriorated sharply, indicating that silicon particles reaching 13.4 μm significantly impair low-temperature performance.

Fig. 4f and Table S4 show the expansion rate of PS1SC&Gr, PS2SC&Gr, PS3SC&Gr and PS4SC&Gr electrodes after lithium intercalation. The electrode swelling rates were 74.52%, 71.20%, 77.89% and 79.56% in the fully lithiated state of 5 mV, respectively. The expansion rates of the electrode were 27.05%, 35.40%, 28.56% and 23.31% in the state of complete delithiation at 2 mV, respectively. The difference in the expansion rate between the lithiated state (5 mV) and the delithiated state (2 V) represents the true expansion rate of the electrode in the lithiated state, which are 47.48%, 35.80%, 49.33% and 56.25%, respectively. It can be seen that the expansion rate of PS2SC&Gr electrode is smaller than that of PS1SC&Gr, PS3SC&Gr and PS4SC&Gr electrodes, which shows that the particle size of 8.4 μm is beneficial to reduce the volume change of Si/C material during lithiation process. This helps the maintain the integrity of the Si/C composites during cycling.

To explore the electrochemical behavior of electrodes made of Si/C materials with different particle sizes more deeply, we evaluated the long-term cycling stability of PS1SC&Gr, PS2SC&Gr, PS3SC&Gr and PS4SC&Gr electrodes at higher current of 0.5 C. In Fig. 4g and 4h, it can be seen that the capacity retention rate of PS3SC&Gr and PS4SC&Gr electrodes with larger particle size is only 65.93% and 58.03% after 100 cycles, and the capacity decay of the battery is extremely fast. Especially, PS4SC&Gr electrode experienced a drop in Coulombic efficiency below 99% after 62 cycles, accompanied by an increase in irreversible side reactions, leading to the fastest perform-

ance degradation among all samples. In contrast, PS1SC&Gr and PS2SC&Gr electrodes with smaller particle size can still reach 77.41% and 79.75% capacity retention after 100 cycles, and Coulombic efficiency is near 99.5%, showing excellent cycling performance. This excellent cycling performance can be attributed to the low swelling ability and faster electrochemical kinetics caused by the smaller particle size of PS1SC and PS2SC.

Overall, following a comprehensive evaluation of physical properties, lithium-intercalation/deintercalation kinetics, high-temperature side reactions, low-temperature kinetics, expansion rate and cycling stability, the 8.4 μm PS2SC demonstrated the most balanced and optimal overall performance.

The coin-cell data indicate that the PS2SC anode exhibits the highest cycling retention and the lowest volume expansion among comparable materials. To evaluate its practical viability, a composite anode (550 mAh g^{-1}) was prepared by blending PS2SC with commercial graphite, paired with a high-load NCM523 cathode, and assembled into a laminated punch cell (Model 235 065, Fig. 5a). In Figure 5b, the formation steps (Step I, II and III) and the capacity grading steps (Step IV and V) are presented. The pouch cell shows a charge capacity of 1028 mAh and a discharge capacity of 879 mAh, corresponding to an ICE value of 85.5%. In the rate-charging tests (Fig. 5c−d), the charging current was progressively increased from 0.2 to 3 C under constant-current mode. Once the voltage reached 4.2 V at each respective current rate, constant-voltage charging was applied and maintained at 4.2 V until the designated cutoff current was reached, the resulting CC/(CC+CV) ratios were 98.4%, 95.7%, 90.16%, 83.8% and 80.7%, respectively, with 80.7% of capacity delivered in the constant-current phase at 3 C, reflecting the fast lithiation kinetics of PS2SC. Similarly, during rate-discharge testing (Fig. 5e and 5f), capacity retentions reached 95.4% at 1 C, 92.4% at 2 C, and 91.2% at 3 C. Even at 3 C, over 90% of the capacity was retained, and the median discharge voltage shifted only 0.183 V (from 3.548 V at 0.2 C to 3.365 V at 3 C), confirming rapid delithiation capability[42−43]. The assembled punch cell was subjected to cycle testing at high currents of 1 C and 3 C, respectively (Fig. 5g-j). The test found that under the condition of 1 C current cycling (Fig. 5g), the punch cell still maintains a Coulombic efficiency of near 100% and a capacity retention rate of 87.46% after 1000 cycles. After 1000 cycles, the punch cell exhibited only 7.83% expansion (Fig. 5h). The low expansion combined with high capacity retention demonstrates excellent structural stability over long-term cycling. To further evaluate the fast kinetics of the Si/C composite, the charge-discharge rate was increased to 3 C (Fig. 5i). Under this condition, the punch cell still maintains a Coulombic efficiency near 100% and 81.49% capacity retention after 1000 cycles, with a minimal expansion rate of 9.02% (Fig. 5j). These results confirm that the material preserves high structural integrity and cycling endurance even during rapid (de)lithiation processes. Notably, the pouch cell exhibits much better cycling stability than coin cells, which may be attributed to the following factors: (1) The pouch cell avoids lithium metal side reactions, such as lithium dendrite growth and dead lithium formation. (2) The pouch cell possesses much lower internal resistance (mΩ level vs. Ω level in coin cells). (3) The slurry preparation process of pouch cells is significantly superior to that of coin cells, ensuring a more stable conductive network. (4) The designed anode specific capacity of the pouch cell is 550 mAh g^{-1}, which is far lower than that of coin cells and reduces silicon-induced volume expansion. (5) The limited operating potential window and N/P ratio above 1 could restrict the (de)lithiation depth, thus alleviating the structural degradation of Si/C composites.

Overall, the particle size of Si/C materials is critical to their performance. A suitable particle size can not only effectively accelerate the reaction kinetics of the battery, but also significantly reduce the occurrence of side reactions in the battery. In addition, effectively controlling the particle size of porous carbon in experiments and commercial production can inhibit the volume expansion of vapor-phase Si/C an-

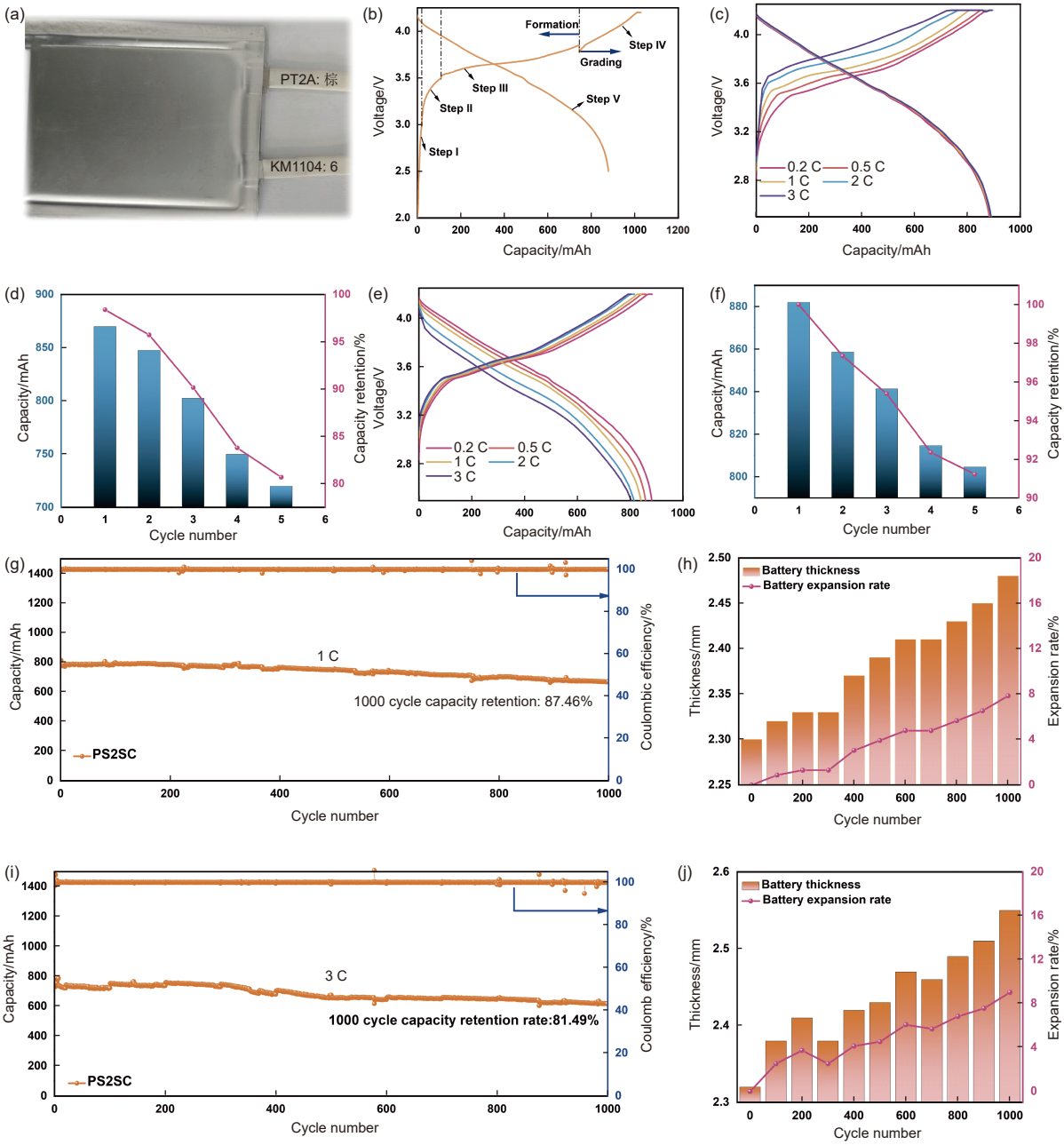

Fig. 5 (a) Photograph of the pouch cell. (b) Formation, capacity separation, and first-charge profile of the pouch cell. (c) Rate-charge curves of the pouch cell employing the PS2SC material. (d) Capacity retention of the pouch cell based on PS2SC material. (e) Pouch cell rate discharge curve of PS2SC material. (f) Rate discharge galvanostatic capacity retention curve of punch cell with PS2SC material. (g, h) are 1000 cycles and expansion performance curves of the PS2SC material after assembling as a full cell at 1 C current, respectively. (i, j) 1000 cycles and expansion performance curves of the PS2SC material after assembling as a full cell at 3 C current, respectively.

ode materials to a certain extent, and the corresponding Si/C materials can also have excellent cycle stability.

4 Conclusion

In summary, this work proposes a scalable kilogram-scale synthetic route for the synthesis of high-performance Si/C composite anodes via silane-based CVD on resin-based porous carbon framework. The abundant micropores (~ 1.9 nm) inside the PCS framework effectively nano-confined the amorphous silicon growth region, resulting in materials with ultra-high capacity (2179 $mAhg^{-1}$), high ICE (93.5%), and low surface area (1.32 $m^2 g^{-1}$). In addition, the mi-

cron-scale optimization of the carbon framework further enhances the reaction kinetics and integrity of the Si/C electrode, providing balanced rate performance (97.0% retention rate at 3 C vs. 0.1 C) and cycle stability (80% retention rate in 100 cycles). When integrated into a practical 879 mAh pouch (550 mAh g^{-1} graphite hybrid anode paired with NCM523), the anode exhibited fast kinetics and excellent long-term durability (87.46% retention after 1000 cycles at 1 C). Moreover, the battery expansion rate after 1000 cycles is lower than 8%, showing extraordinary practicality. The synergistic combination of nanoscale confinement, amorphous silicon, and micron-scale structural control provides a scalable strategy for the development of next-generation Si/C anodes for lithium-ion batteries.

References

[1] Kim N, Kim Y, Sung J, et al. Issues impeding the commercialization of laboratory innovations for energy-dense Si-containing lithium-ion batteries[J]. Nature Energy, 2023, 8: 921-933.

[2] Chen Z, Soltani A, Chen Y, et al. Emerging organic surface chemistry for Si anodes in lithium-ion batteries: advances, prospects, and beyond[J]. Advanced Energy Materials, 2022, 12: 2200924.

[3] Li H, Huang X J, Chen L Q, et al. A high capacity nano-Si composite anode material for lithium rechargeable batteries[J]. Electrochemical and Solid-State Letters, 1999, 2: 547.

[4] Chan C K, Peng H, Liu G, et al. High-performance lithium battery anodes using silicon nanowires[J]. Nature Nanotechnology, 2008, 3: 31-35.

[5] Sharma R A, Seefurth R N. Thermodynamic properties of the lithium-silicon system[J]. Journal of The Electrochemical Society, 1976, 123: 1763-1768.

[6] Choi S, Kwon T, Coskun A, et al. Highly elastic binders integrating polyrotaxanes for silicon microparticle anodes in lithium ion batteries[J]. Science, 2017, 357: 279-283.

[7] Kovalenko I , Zdyrko B, Magasinski A, et al. A major constituent of brown algae for use in high-capacity Li-ion batteries[J]. Science, 2011, 334: 75-79.

[8] Qiu S, Ji K, Zhang Y, et al. Multidimensional strategies for enhancing silicon-system anodes in lithium-ion batteries: From half cells to full cells[J], ACS Applied Materials & Interfaces, 2026, 18: 333-3359.

[9] Liu X H, Zhong L, Huang S, et al. Size-dependent fracture of silicon nanoparticles during lithiation[J]. ACS Nano, 2012, 6: 1522-1531.

[10] Huo H, Janek J, Silicon as emerging anode in solid-state batteries[J]. ACS Energy Letters, 2022, 7: 4005-4016.

[11] Ma D D D, Lee C S, Au F C K, et al. Small-diameter silicon nanowire surfaces[J]. Science, 2003, 299: 1874-1877.

[12] Kim G, Yang M J, Lee S, et al. Comparison between crystalline and amorphous silicon as anodes for lithium ion batteries: Electrochemical performance from practical cells and lithiation behavior from molecular dynamics simulations[J]. Materials, 2025, 18: 515.

[13] Wild J F, Li Y, Zhou Y, et al. Micron-sized nanostructured Si–C composites for high-performance Li-ion battery anodes[J]. ACS Applied Nano Materials, 2025, 8: 21840-21848.

[14] Zhang X, Kong D, Li X, et al. Dimensionally designed carbon-silicon hybrids for lithium storage[J]. Advanced Functional Materials, 2018, 29: 1806061.

[15] Kim S Y, Lee J, Kim B H, et al. Facile Synthesis of carbon-coated silicon/graphite spherical composites for high-performance lithium-ion batteries[J]. ACS Applied Materials & Interfaces, 2016, 8: 12109-12117.

[16] Liu N, Lu Z, Zhao J, et al. A pomegranate-inspired nanoscale design for large-volume-change lithium battery anodes[J]. Nature Nanotechnology, 2014, 9: 187-192.

[17] Li J Y, Li G, Zhang J , et al. Rational design of robust Si/C microspheres for high-tap-density anode materials[J]. ACS Applied Materials & Interfaces, 2019, 11: 4057-4064.

[18] Magasinski A, Dixon P, Hertzberg B, et al. High-performance lithium-ion anodes using a hierarchical bottom-up approach[J]. Nature Materials, 2010, 9: 353-358.

[19] Lee Y , Hong S C, Kim K, et al. Kang, Multiscale carbon-integrated silicon anode for stable cycling under practical lithium-ion battery conditions[J]. Advanced Energy Materials, 2025, e04250.

[20] Xiao Z, Wu H, Quan L, et al. Micro-sized CVD-derived Si-C anodes: challenges, strategies, and prospects for next-generation high-energy lithium-ion batteries[J]. Energy & Environmental Science, 2025, 18: 4037-4052.

[21] Zhao Z, Chen F, Han J, et al. Yang, Revival of microparticular silicon for superior lithium storage[J]. Advanced Energy Materials, 2023, 13: 2300367.

[22] Li H, Li H , Lai Y, et al. Revisiting the preparation progress of nano-structured Si anodes toward industrial application from the perspective of cost and scalability[J]. Advanced Energy Materials, 2022, 12: 2102181.

[23] Jiang Z, Shen L, Lu J, et al. Fluidization synthesis of silicon-nanocrystals embedded mesoporous carbon for high-performance lithium-ion batteriess[J]. Carbon, 2025, 245: 120849.

[24] Mu X , Xu X, Xu H, et al. Optimizing the pore structure in silicon–carbon anodes: the impact of micropore and mesopore ratios on electrochemical performance[J]. Journal of Materials Chemistry A, 2025, 13: 17699-17708.

[25] He J, Deng Y, Han J, et al. Sieving pore design enables stable and fast alloying chemistry of silicon negative electrodes in Li-ion batteries[J]. Nature Communications, 2025, 16: 4858.

[26] Chen B, Chen L, Zu L, et al. Zero-Strain High-capacity silicon/carbon anode enabled by a MOF-derived space-confined single-atom catalytic strategy for lithium-ion batteries[J]. Advanced Materials, 2022, 34: 2200894.

[27] Xu J, Yin Q, Li X, et al. Spheres of graphene and carbon nanotubes embedding silicon as mechanically resilient anodes for lithium-ion batteries[J]. Nano Letters, 2022, 22: 3054-3061.

[28] Rathore D, Abraham J J, Mendel-Elias E, et al. Characterizing structure and electrochemical properties of advanced Si/C anode materials[J]. Journal of The Electrochemical Society, 2025, 172: 010504.

[29] McDowell M T, Lee S W, Harris J T, et al. In situ TEM of two-phase lithiation of amorphous silicon nanospheres[J]. Nano Letters, 2013, 13: 758-764.

[30] Liu X H , Zhong L, Huang S, et al. Size-dependent fracture of silicon nanoparticles during lithiation[J]. ACS Nano, 2012 6: 1522-1531.

[31] Antonyuk S, Tomas J, Heinrich S, et al. Breakage behaviour of spherical granulates by compression[J]. Chemical Engineering Science, 2005, 60: 4031-4044.

[32] Lee Y, Hong S C, Kim K, et al. Multiscale carbon-integrated silicon anode for stable cycling under practical lithium-ion battery conditions[J]. Advanced Energy Materials, 2025, e04250.

[33] Li H, Chen Z, Kang Z, et al. High-density crack-resistant Si-C microparticles for lithium ion batteries[J]. Energy Storage Materials, 2023, 56: 40-49.

[34] Liu P, Yang L, Xiao B, et al. Revealing lithium battery gas generation for safer practical applications[J]. Advanced Functional Materials, 2022, 32: 2208586.

[35] Hu J, Li L, Qiu K, et al. Rational design of multi-salt propylene carbonate-based electrolyte for enhanced long-lifespan and safety in pouch cells[J]. Chemical Engineering Journal, 2025, 518: 164639.

[36] Hu L, Jin M, Zhang Z, et al. Interface-adaptive binder enabled by supramolecular interactions for high-capacity Si/C composite anodes in lithium-ion batteries[J]. Advanced Functional Materials, 2022, 32: 2111560.

[37] Chen S, Zhu H, Li J, et al. Tailoring sodium carboxymethylcellulose binders for high-voltage $LiCoO_2$ via thermal pulse sintering[J]. Angewandte Chemie International Edition, 2025, 64: e202423796.

[38] Xu Q, Guo L, Zhang Y, et al. Revealing carbon intermediate structure and functions for carbon-coated silicon anodes[J]. Advanced Functional Materials, 2025, e30635.

[39] Li J, Dahn J R. An in situ X-Ray diffraction study of the reaction of Li with crystalline Si[J]. Journal of The Electrochemical Society, 2007, 154: A156.

[40] You Z, Lin C, Zheng P, et al. Fluorine-doping carbon-modified Si/SiO_x to effectively achieve high-performance anode[J]. Small, 2025, 21: 2407215.

[41] Xie Y, Feng X, Wang Y, et al. Thermochemical crosstalk in Si-C anodes: mechanism and stabilization via a polymerizable phosphorus-based additive[J]. Advanced Energy Materials, 2025, e04167.

[42] Zhou L, Fan X, Du H, et al. Ultra-stable high-voltage cycling of Li-ion batteries via interphase engineering with 3, 5-bis(trifluoromethyl)phenyl isocyanate[J]. Advanced Functional Materials, 2026, e23184.

[43] Yang J, Zhang Y, Zhang W, et al. 4f-orbital-induced electron delocalization of $TiNb_2O_7$ enables low temperature fast-charging Ah-level pouch cell[J]. Energy Storage Materials, 2026, 84: 104851.